

Genome-wide analysis of the interplay between chromatin-associated RNA and 3D genome organization in human cells

Received: 17 May 2023

Accepted: 5 October 2023

Published online: 16 October 2023

 Check for updates

Riccardo Calandrelli^{1,7}, Xingzhao Wen^{2,7}, John Lalith Charles Richard ^{1,7}, Zhifei Luo ^{1,8}, Tri C. Nguyen¹, Chien-Ju Chen², Zhijie Qi ¹, Shuanghong Xue¹, Weizhong Chen¹, Zhangming Yan¹, Weixin Wu¹, Kathia Zaleta-Rivera¹, Rong Hu^{3,4}, Miao Yu⁴, Yuchuan Wang⁵, Wenbo Li ⁶, Jian Ma ⁵, Bing Ren ^{3,4} & Sheng Zhong ¹ 

The interphase genome is dynamically organized in the nucleus and decorated with chromatin-associated RNA (caRNA). It remains unclear whether the genome architecture modulates the spatial distribution of caRNA and vice versa. Here, we generate a resource of genome-wide RNA-DNA and DNA-DNA contact maps in human cells. These maps reveal the chromosomal domains demarcated by locally transcribed RNA, hereafter termed RNA-defined chromosomal domains. Further, the spreading of caRNA is constrained by the boundaries of topologically associating domains (TADs), demonstrating the role of the 3D genome structure in modulating the spatial distribution of RNA. Conversely, stopping transcription or acute depletion of RNA induces thousands of chromatin loops genome-wide. Activation or suppression of the transcription of specific genes suppresses or creates chromatin loops straddling these genes. Deletion of a specific caRNA-producing genomic sequence promotes chromatin loops that straddle the interchromosomal target sequences of this caRNA. These data suggest a feedback loop where the 3D genome modulates the spatial distribution of RNA, which in turn affects the dynamic 3D genome organization.

The interphase genome is highly organized¹. The multiscale organizational features of the genome have been characterized, including A/B compartments², topologically associating domains (TADs)^{3,4}, and chromatin loops⁵. This multiscale organization begs the question of what the functions of such an intricate architecture are. Transcriptional regulation is one of the possible functions and the most extensively studied function. In this direction, the genome architecture is

shown to regulate the transcription of specific genes^{1,6,7}, but it remains debatable whether the genome architecture has a widespread role in modulating the transcription of many genes⁸. Moreover, it remains unclear if the 3D genome's regulatory roles are limited to transcriptional regulation. Other possible functions have rarely been tested. Here, we test another possible function, namely regulating spatial localization of chromatin-associated RNA (caRNA)⁹.

¹Shu Chien-Gene Lay Department of Bioengineering, University of California San Diego, La Jolla, CA, USA. ²Bioinformatics and Systems Biology Program, University of California San Diego, La Jolla, CA, USA. ³Department of Cellular and Molecular Medicine, Center for Epigenomics, University of California San Diego, La Jolla, CA, USA. ⁴Ludwig Institute for Cancer Research, La Jolla, CA, USA. ⁵Computational Biology Department, School of Computer Science, Carnegie Mellon University, Pittsburgh, PA, USA. ⁶Department of Biochemistry and Molecular Biology, McGovern Medical School, University of Texas Health Science Center, Houston, TX, USA. ⁷These authors contributed equally: Riccardo Calandrelli, Xingzhao Wen. ⁸These authors jointly supervised this work: John Lalith Charles Richard, Zhifei Luo. ✉e-mail: szhong@ucsd.edu

After initial debates⁹, caRNA has been recognized as an integral component of interphase chromosomes rather than passive degradation products^{10–14}. Growing evidence confirms that caRNA regulates gene transcription and RNA splicing^{15–26}. These regulatory roles often depend on caRNA's spatial localization within the nucleus^{20,27–30}. Depending on their spatial localizations, caRNAs can orchestrate the organization of nuclear bodies and compartments^{29–32} and foster the formation of transcriptionally silent or active chromosomal domains^{30,33,34}. However, it remains unclear how the caRNAs are spatially organized in the context of the multiscale genome architecture; whether there is any specificity in the spatial distribution of caRNAs; if there is, how is such specificity regulated; and in turn, whether the spatial localization of caRNA modulates the dynamic organization of the genome.

Guided by these questions, we generate high-resolution genome-wide RNA-DNA contact maps^{15,35–38} in human cells using *in situ* Mapping of RNA-Genome Interaction (iMARGI)^{35,36}. iMARGI captures RNA-genome associations by jointly sequencing caRNAs and their associated genomic sequences with paired-end sequence reads³⁵. iMARGI can differentiate the sequencing reads originating from RNA (iMARGI RNA-end reads) or genomic DNA (iMARGI DNA-end reads). We also use *in situ* Hi-C (Hi-C)^{5,39} to map genome-wide chromatin interactions. These maps reveal that most caRNAs are associated with the genomic sequences within several megabases of their transcription sites.

To dissect any causal relationships between the 3D genome organization and caRNA, we generate RNA-DNA contact maps in the genetically engineered human cells where the TAD boundaries are deleted or inserted. Comparisons of these maps reveal the ability of TAD boundaries to constrain the spreading of caRNA on the chromosomes. These data demonstrate the 3D genome's functions in regulating the spatial localization of the caRNA. Moreover, we generate RNA-DNA and DNA-DNA contact maps in human cells undergone either acute RNA depletion or deletion of a specific caRNA-producing sequence. These data reveal a suppressive role of between-anchor caRNA, i.e., the caRNA associated with the genomic region between the loop anchors, on chromatin looping. Thus, the spatial localization of the caRNA, in turn, modulates the dynamic 3D genome organization.

Results

Localized RNA-genome association and RNA-defined chromatin domains

We generated iMARGI data from human embryonic stem (H1), foreskin fibroblast (HFF), and chronic myelogenous leukemia (K562) cells in duplicates (Table S1). These data revealed the relative level of any gene's RNA attached to any genomic region (target region), hereafter called the RNA attachment level (RAL) of this gene in the target region, defined as the number of iMARGI read pairs with the RNA ends mapped to this gene and the DNA ends mapped to this target region³⁵. For example, in H1 ES cells the coding gene *Jumonji* and AT-Rich Interaction Domain Containing 2 (*JARID2*) exhibited large RAL in an approximately 5 Mb region containing the *JARID2* gene (Fig. 1a). Additionally, the non-coding gene *Pvt1* Oncogene (*PVT1*) exhibited large RAL in an approximately 7 Mb region containing the *PVT1* gene (Fig. 1b). Overall, the average RAL of all the genes decreases as the genomic distance between the gene and the target region increases (Supplementary Fig. S1a).

We represented iMARGI data as a contact matrix, where the rows represent the RNA ends of iMARGI read pairs, and the columns represent the corresponding DNA ends³⁶ (Fig. 1c). A notable difference to Hi-C's symmetric contact matrix is that iMARGI's contact matrix is asymmetric. This is because RNA-DNA contacts are not necessarily reciprocal. Rectangular blocks of high-value entries emerged as a recurring pattern from iMARGI's contact matrix (Fig. 1c). We identified the rectangular blocks using HOMER⁴⁰ to call peaks on the rows of the contact matrix (row peaks), and in each row peak using HOMER to call

one strongest peak in the columns (column peak). A pair of row peak and column peak defines a rectangular block. We identified 3217, 2019, and 2468 rectangular blocks from H1, HFF, and K562 iMARGI data (Fig. 1d). All the identified rectangular blocks overlap with the diagonal entries of iMARGI's contact matrix, suggesting that they represent localized RNA-genome associations where a RNA's target regions are near the transcription site of this caRNA. Each rectangular block corresponds to a unique chromatin domain, characterized by extensive genomic association of the RNA transcribed from within this domain. Hereafter we term such domains "RNA-association domains". The size of an RNA-association domain, represented by the width of a rectangular block, can reach tens of megabases (Fig. 1e). In summary, RNA-association domains emerged as a main feature of the genome-wide distributions of caRNA.

Correlation between 3D genome compartmentalization and RNA-chromatin association

The 3D genome is organized on different scales, including compartments, TADs, and chromatin loops¹. We asked whether the RNA association on any genomic region correlates with this genomic region's 3D compartmentalization. To this end, we generated Hi-C data in H1, HFF, and K562 cells in duplicates and compared them with our iMARGI data (Table S1). We calculated the cumulative RAL (cRAL), the sum of the RAL of all the RNA, on every genomic region, defined as the number of iMARGI read pairs with the DNA ends mapped to this genomic region³⁵. The A/B compartments as indicated by Hi-C contact matrix's first eigenvector (PC1)⁴¹ exhibited a genome-wide correlation with cRAL (p -value < $2e-16$, one way ANOVA), revealing a correlation between 3D genome compartmentalization and RNA-chromatin association.

We asked if the higher cRAL in the A compartment is completely attributable to a higher level of local transcription. To this end, we compared *JARID2* and *PVT1*'s RALs with A/B compartments⁴¹ (PC1 track, Fig. 1a, b). Both *JARID2* and *PVT1* exhibited small but non-zero RALs in several A compartment genomic regions that are tens of megabases away from the *JARID2* and *PVT1* genes (Fig. 1a, b). However, the B compartment genomic regions that are closer to the *JARID2* and *PVT1* genes did not exhibit association of *JARID2* or *PVT1* RNA (Fig. 1a, b), suggesting an enrichment of target regions of long-range RNA-chromatin contacts in the A compartment. Thus, the higher cRAL in the A compartment is not completely due to a higher level of local transcription.

TAD boundaries insulate RNA-DNA contacts

TADs, where DNA sequences interact with each other more frequently than with the sequences outside, are important 3D genome features that are strongly correlated with transcriptional regulation^{3,4}. We separately analyzed the RNA transcribed from within a TAD or the other regions of the same chromosome outside of this TAD. The chromatin attachment level of any RNA transcribed from within a TAD sharply decreases at the two boundaries of this TAD (p -value = $6.5e-16$, Wilcoxon rank-sum test) (Fig. 2a). Conversely, the attachment level of any RNA transcribed from outside of a TAD exhibits drastic changes at the TAD boundaries in the opposite direction (p -value = $2.6e-12$, Wilcoxon rank-sum test) (Supplementary Fig. S1b). These changes at TAD boundaries cannot be completely explained by the 1-dimensional genomic distance to the caRNA's transcription site. They suggest the possibility that a TAD boundary can insulate RNA-DNA contacts from the two sides of this boundary (cross-over RNA-DNA contacts).

We asked if altering the genomic sequence within a TAD boundary can affect the cross-over RNA-DNA contacts. First, we leveraged our previous finding that a CRISPR-mediated deletion of a HERV-H element (Chr13:55,578,227–55,584,087) (KO) within a TAD boundary from H9 human ES cells (WT) abolishes this TAD boundary⁴². We carried out iMARGI experiments on the KO and WT cells. We counted the numbers of cross-over and non-cross-over iMARGI read pairs in WT and KO.

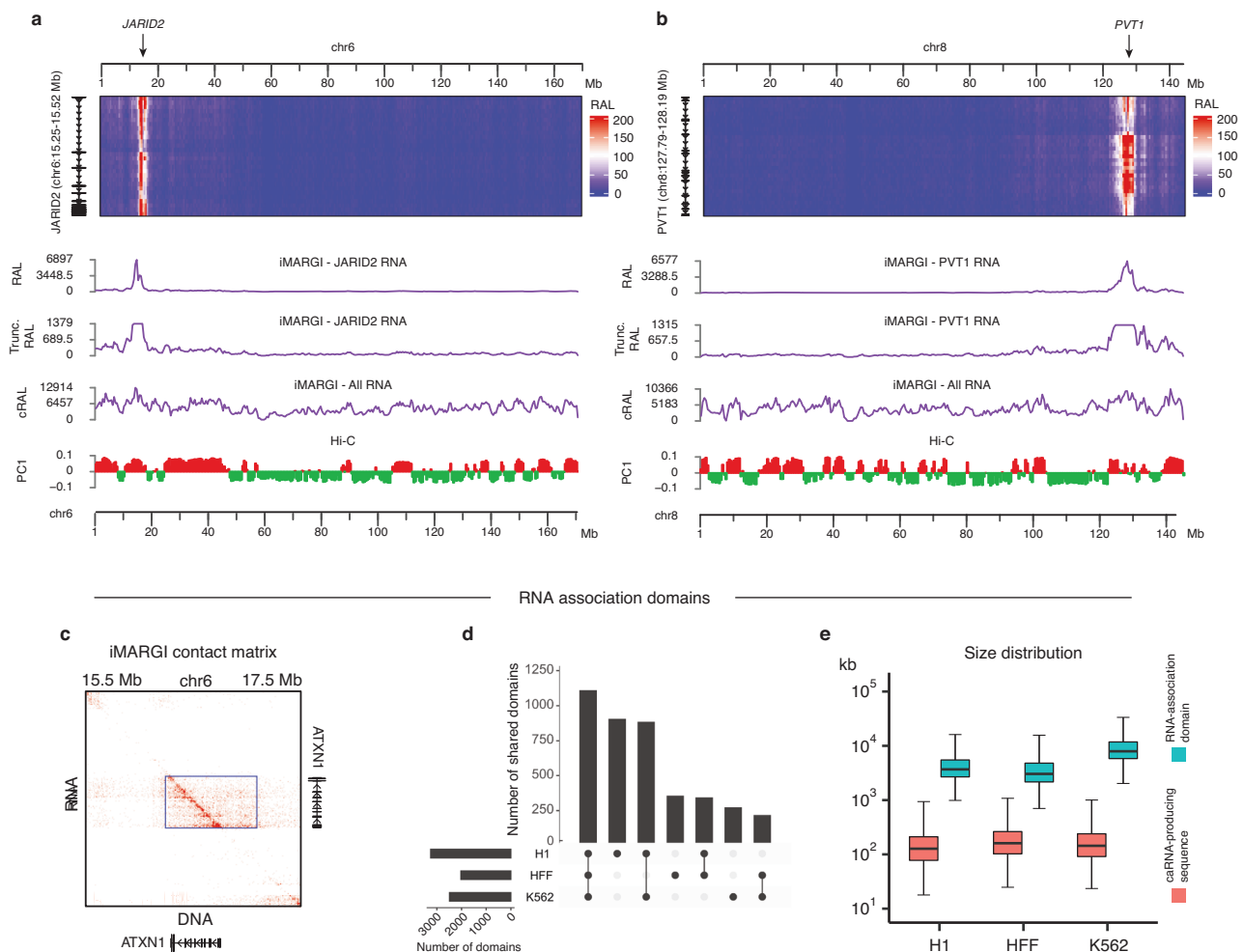


Fig. 1 | Localized RNA-genome association. **a** iMARGI's contact matrix between the RNA of the JARID2 gene (rows, bin size = 10 kb) to the genomic sequence of chromosome 6 (columns, bin size = 500 kb). The RNA association level (RAL) of JARID2 RNA (RAL track), the truncated version of RAL showing the small values (Trunc. RAL track), and the cumulative RAL of all RNA (cRAL track) exhibit a correlation with the first principal component of Hi-C's contact matrix (PC1 track). **b** iMARGI's contact matrix, RAL, and truncated RAL of the PVT1 RNA on chromosome 6. **c** An RNA-DNA contact matrix in a 2 Mb sequence on Chromosome 6. Each entry in this contact matrix represents the number of iMARGI read pairs with the RNA-end mapped to the corresponding row and the DNA-end mapped to the corresponding column. The box marks an identified RNA-association domain, an approximately 1 Mb region containing the ATXN1 gene. **d** Upset plot of the

numbers of the detected RNA-association domains in H1, HFF, and K562. **e** Box plots of RNA-association domains' sizes (blue) corresponding to the widths of the detected rectangular blocks, and the lengths of caRNA-producing genomic sequences (red) for each RNA-association domain corresponding to the heights of the detected rectangular blocks in iMARGI's contact matrix ($n = 3,217$ RNA-association domains). The center line of the boxplots is the median. The lower and upper hinges correspond to the first and third quartiles (the 25th and 75th percentiles). The upper whisker extends from the hinge to the largest value no further than $1.5 \times$ IQR from the hinge (where IQR is the inter-quartile range, or distance between the first and third quartiles). The lower whisker extends from the hinge to the smallest value at most $1.5 \times$ IQR of the hinge. Source data are provided as a Source Data file.

Compared to WT, KO exhibited an increased proportion in the cross-over read pairs (OR = 1.3, p -value = 0.013, Chi-square test) (Fig. 2b, c, g). Thus, deleting a fraction of a TAD boundary reduced its insulation to cross-over RNA-DNA contacts.

Second, we previously created an insertion cell line (KI) using piggyBac transposon-mediated genomic insertion of this HERV-H sequence and identified seven insertion sites in KI⁴² (Columns, Fig. 2d). Four of the seven insertion sites exhibited small increases in insulation (unlikely-de_novo-boundary sites), as measured by the difference in directionality index ($\Delta_{DI} < 20$) (Columns 4–7, Fig. 2d), whereas the other three insertion sites exhibited large increases in insulation ($\Delta_{DI} > 20$, likely-de_novo-boundary sites)⁴² (Columns 1–3, Fig. 2d). Only one insertion site, that has the largest increase in insulation ($\Delta_{DI} = 66.3$), reached the significance level to be detected as a de novo TAD boundary, i.e., a boundary called in the KI Hi-C but not called in the WT Hi-C (de_novo-boundary site) (Column 1, Fig. 2d). We note the de_novo-boundary site is one of the three likely-de_novo-boundary sites.

To test any impact of any insertion site on RNA-DNA contacts, we carried out iMARGI in KI and WT cells. For every insertion site, our null hypothesis is that whether any RNA-DNA contact is a cross-over or a non-cross-over contact is independent of whether this RNA-DNA contact is detected in KI or WT. The three likely-de_novo-boundary sites ($\Delta_{DI} > 20$) all led to some degrees of decrease in the odds ratio (OR) of the cross-over RNA-DNA contacts in KI (OR < 0.90), in which the decreases on two of the three likely-de_novo-boundary sites were significant (p -value < 1.0×10^{-4} , Chi-square test, stars in Fig. 2d). In particular, the de_novo-boundary site exhibited a significant decrease in the OR of the cross-over RNA-DNA contacts in KI (OR = 0.75, p -value = 3.7×10^{-5} , Chi-square test, Fig. 2e–g). Thus, the de novo creation of a TAD boundary suppressed cross-over RNA-DNA contacts.

In contrast, none of the four unlikely-de_novo-boundary sites ($\Delta_{DI} < 20$) led to a detectable decrease in the OR of the cross-over RNA-DNA contacts in KI (OR > 0.99, p -value > 0.63, Chi-square test,

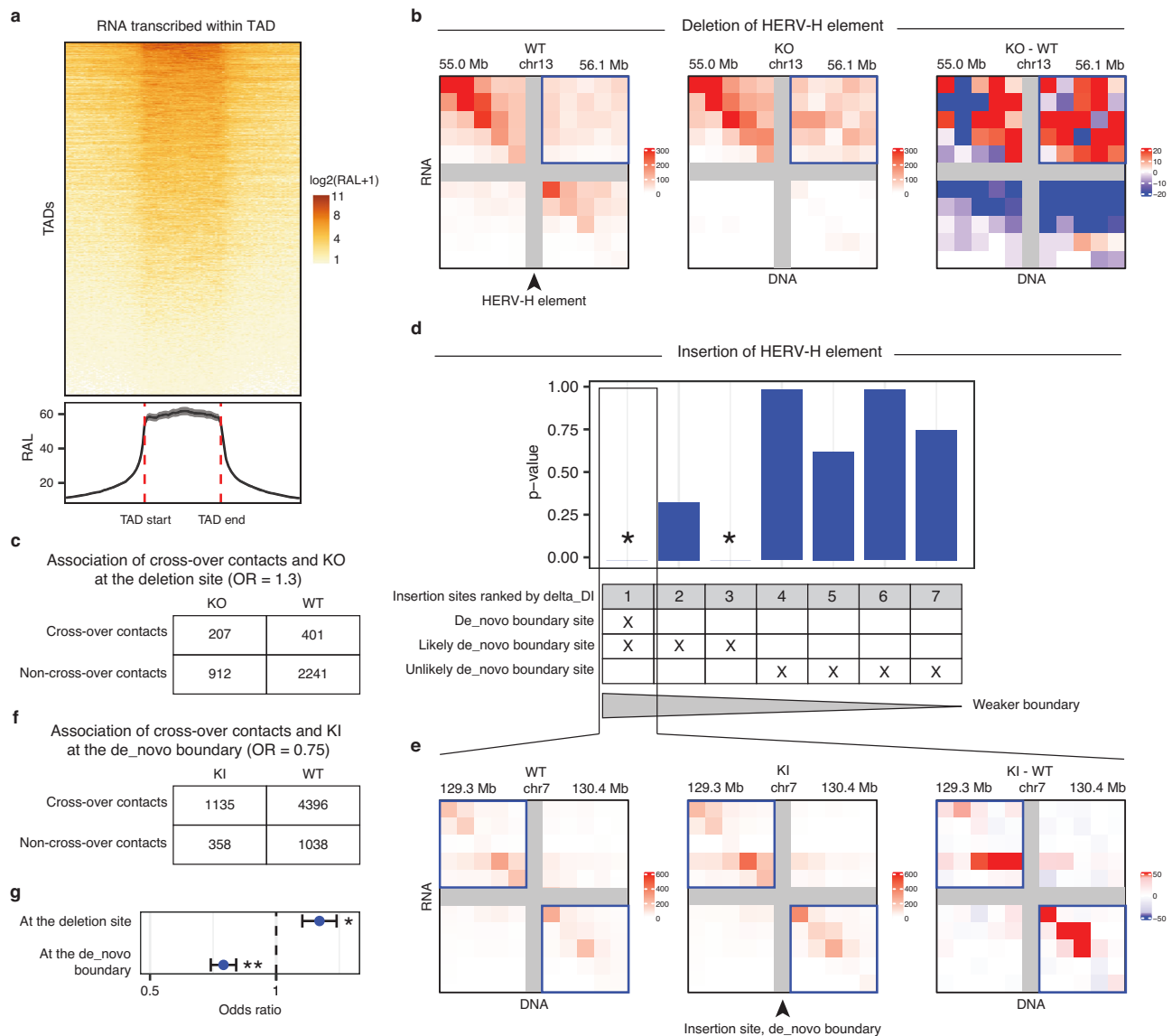


Fig. 2 | TAD boundaries suppress cross-over RNA-DNA contacts. **a** The RNA association level (RAL, color-coded) of the RNA transcribed within each TAD (row) on this TAD (center block) and its equal-length flanking regions (x axis). Curve at the bottom: the average RAL of all TADs (rows) with the 95% confidence interval (band). **b** Comparison of normalized RNA-DNA contact matrices in WT and KO cell lines. The arrowhead points to the HERV-H element in WT that is deleted in KO. KO-WT: The contrast of the KO and WT contact matrices where red indicates an increase of RNA-DNA contacts in KO. The increased RNA-DNA contacts in KO are enriched with cross-over contacts (in the box at the upper right corner). **c** The 2×2 contingency table for an association test based on the data in (b). **d** The seven previously identified insertion sites (columns) are ranked by delta_DI, where a smaller delta_DI (on the right) indicates a smaller increase in the ability to insulate cross-over DNA-DNA contacts (a weaker putative boundary). The rows mark whether each insertion site is a “de_novo boundary site” (Column 1), a “likely-de_novo-boundary site” (Columns 1–3), or an “unlikely-de_novo-boundary site” (Columns 4–7), based on the comparison of Hi-C data in KI and WT. A Chi-square test is

performed on each insertion site (column) based on the iMARGI data in KI and WT. A smaller *p*-value (y axis) represents stronger evidence against the null hypothesis that there is no association between the RNA-DNA cross-over contacts and KI. **p*-value = 3.724e-5. **d**, **e** Comparison of normalized RNA-DNA contact matrices in WT and KI cell lines at the de_novo boundary site (arrowhead). KI-WT: The contrast of the KI and WT contact matrices where red indicates an increase of RNA-DNA contacts in KI. The increased RNA-DNA contacts in KI are enriched in the non-cross-over contacts (in the boxes at the upper left and lower right corners). **f** The 2×2 contingency table for an association test based on the data in (e). **g** Significance levels for the deletion site (b, c) and the de_novo-boundary insertion site (e, f). **p*-value = 0.013, ***p*-value = 3.724e-5, Chi-square test. Data are presented as odds ratios, with the error bar whiskers at $\exp(\log(\text{OR}) \pm \text{SELOG})$, where SELOG is the standard error of the log odds ratio ($n = 3761$ and 6927 RNA-DNA contacts at the deletion and insertion site respectively). Source data are provided as a Source Data file.

Fig. 2d). Thus, inserting the same DNA sequence without sufficient subsequent changes in TAD structure did not suppress the cross-over RNA-DNA contacts. Taken together, these data show an impact of the 3D genome structure to the distribution of caRNA.

Induction of transcription locally suppresses chromatin looping

Our next question is whether RNA has an impact on the 3D structure of the genome. We approached this question in three steps. First, we

depleted RPB1, the largest subunit of RNA Polymerase II (RNAP II), in HCT116 cells. RPB1 depletion resulted in increases in loop number and strengths as measured by Hi-C (Extended Text: RPB1 depletion, Supplementary Information). This result is consistent with the recent report in another cell line (DLD-1), where depletion of RPB1 led to the emergence of chromatin loops⁴³. These data implicate the transcriptional machinery, especially the presence of RNAPII on chromatin, in suppressing chromatin looping.

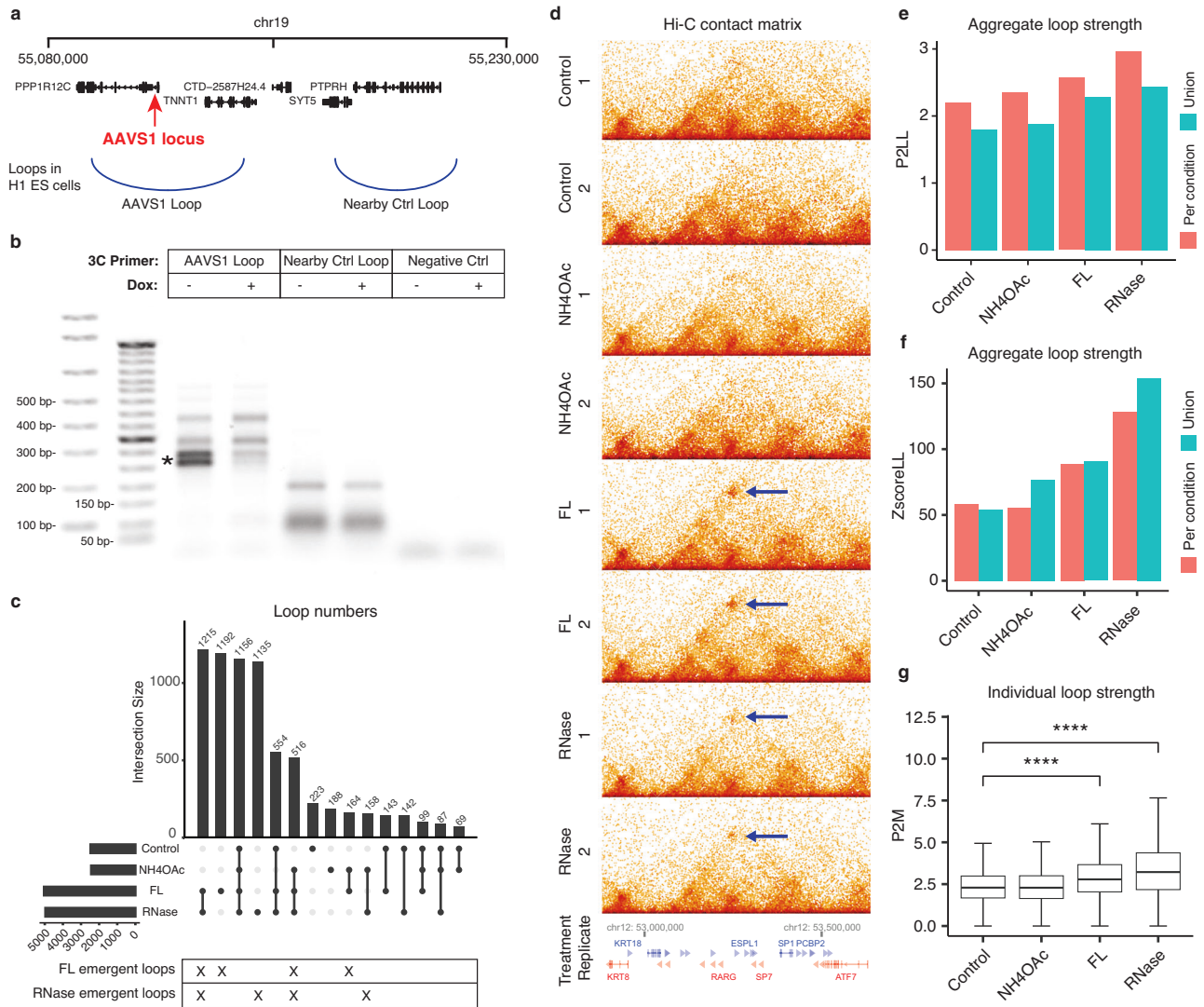


Fig. 3 | RNA-related loop changes. **a** Transcription induction of a gene suppresses a loop straddling this gene. Genomic coordinates of the AAVS1 locus, the loop straddling the AAVS1 locus (AAVS1 loop), and a nearby loop with a similar size (Nearby Ctrl loop). **b** 3C products without doxycycline (Dox: -) and with transcription induction by doxycycline (Dox: +), based on primers against the AAVS1 loop (Lanes 3, 4), the Nearby Ctrl loop (Lanes 5, 6), and a size-matched control region without any Hi-C detected loop (Negative Ctrl, Lanes 7, 8). *: Difference in 3C products between Dox- and Dox+. Lane 1: E-Gel™ 1 kb DNA Ladder. Lanes 2 and 9: E-Gel™ 50 bp DNA Ladder. Each experiment was repeated independently 3 times. **c** Upset plot of the loop numbers in the four conditions, Control, NH4OAc, FL, and RNase (rows). **d** An example of loop changes. Hi-C contact matrix of every replicate (row). Arrows: a shared loop in FL and RNase that is absent in Control and NH4OAc.

e–g FL and RNase increase loop strengths. **e, f** Aggregate loop strength represented by P2LL (**e**) or ZscoreLL (**f**) (y axis) in each condition (column). Color bars: the loops detected in each condition (red) or their union (blue). **g** Box plots of the strengths of individual loops (P2M) in every condition (column). *****p*-value < 2.2e-16, Wilcoxon test (*n* = 6783 loops). The center line of the boxplots is the median. The lower and upper hinges correspond to the first and third quartiles (the 25th and 75th percentiles). The upper whisker extends from the hinge to the largest value no further than 1.5 * IQR from the hinge (where IQR is the inter-quartile range, or distance between the first and third quartiles). The lower whisker extends from the hinge to the smallest value at most 1.5 * IQR of the hinge. Source data are provided as a Source Data file.

Second, we tested if the induction of the transcription of a specific gene suppresses chromatin looping. To this end, we leveraged that there is a ~ 55 kb loop straddling the AAVS1 locus (AAVS1 loop), and nearby, there is a non-overlapping loop with a similar size to the AAVS1 loop⁴⁴ (Nearby Ctrl loop, Fig. 3a). We applied doxycycline to engineered H1 ES cells with a dCas9-KRAB knock-in transgene at the AAVS1 locus⁴⁵ to induce transcription of the transgene at the AAVS1 locus (Dox+), and subsequently tested the loops with chromosome conformation capture (3C)⁴⁶. Compared to without doxycycline (Dox-), Dox+ weakened the AAVS1 loop (star, Fig. 3b) but had little impact on the Nearby Ctrl loop (Fig. 3b). Thus, inducing the expression of a gene can suppress a chromatin loop that straddle across this gene. Taken together, the transcription of a gene can locally suppress chromatin

looping. It remains unclear whether it is the transcriptional machinery, the process of transcription, or the product of transcription, i.e., RNA, that affects chromatin looping.

RNA has a genome-wide impact on chromatin looping

We asked whether it is the transcription (including the association of the transcriptional machinery on chromatin and the process of transcription) or the RNA that impacts chromatin looping. We recognized that we could not answer this question by only testing with a specific genomic locus. This is because the answer at one genomic locus cannot necessarily rule out the alternative answer in other genomic regions. Thus, we recognized that the perhaps more important question is whether transcription or RNA has a genome-wide impact on

chromatin looping. Furthermore, we recognized that if RNA impacts chromatin looping, then the transcriptional process must be implicated. However, if the transcriptional process is the cause, the causal chain does not necessarily involve RNA. With these considerations, we revised our question to whether RNA can impact chromatin looping genome-wide. To answer this question, we compared chromatin looping in control, transcription-inhibited^{47–49}, and RNase-treated cells⁵⁰. If the primary cause is the transcription process, we expect to see a widespread impact in transcription inhibition but not in acute RNase treatment. However, if transcription inhibition and acute RNase treatment lead to overlapping changes in chromatin loops genome-wide, the data would suggest RNA is involved in modulating chromatin looping. Additionally, we included another experimental condition where electrostatic molecular interactions are inhibited to test if any observed impacts are attributable to charge-driven condensates or phase separation^{51,52}.

In our third step, we subjected H1 cells to ammonium acetate (NH₄OAc) to disrupt electrostatic molecular interactions (the interactions due to electric charges)^{51–53}, flavopiridol (FL) to suppress transcription elongation without displacing RNAPII from chromatin^{47–49,54}, and acute RNase treatment to reduce RNA in the nuclei (10-minute RNase treatment before fixing the cells)⁵⁰ based on established protocols (NH₄OAc⁵¹, FL⁴⁷, RNase A⁵⁰). NH₄OAc disrupts molecular electrostatic interactions in living cells by providing monovalent cations without perturbing intracellular pH⁵². To check the expected effects of the three treatments, we immunostained nuclear speckle-associated proteins SON⁵⁵ and SC35⁵⁶ in control and each treatment. NH₄OAc reduced the numbers of SON and SC35's foci (p -value = 0.001 for SON, 0.009 for SC35, Wilcoxon test) (Supplementary Fig. S2a, b, e, f, i, l), consistent with the role of RNA's electrostatic interactions in maintaining nuclear speckles⁵⁷. Conversely, FL made SON and SC35 foci larger and more distinct⁵⁸ (Supplementary Fig. S2c, g, j, m). RNase A increased the numbers of SON and SC35's foci (p -value = 0.034 for SON, 0.010 for SC35, Wilcoxon test) (Supplementary Fig. S2d, h, k, n), consistent with the observations that "low RNA/protein ratios promote phase separation into liquid droplets"⁵⁹ and condensate formation⁶⁰.

We generated Hi-C data after each treatment in duplicates (Table S1) and analyzed these data together with those of the unperturbed H1 cells (control). We called chromatin loops from our Hi-C data in each of the four conditions that have comparable sequencing depths (Table S1) using HiCCUPS⁶¹. The loop numbers were similar in Control (2473 loops) and NH₄OAc (2437 loops) (p -value = 0.55, paired t test) and were increased in FL (5,039 loops) (p -value < 1.1e-8, paired t test) and RNase (4963 loops) (p -value < 2.3e-9, paired t-test) (Fig. 3c). These loop number differences cannot be attributed to different sequencing depths or batch effects because the samples were prepared in the same batch and sequenced to comparable depths (600–650 million read pairs per condition, Table S1b). Most of the emerged loops in FL colocalized with the emerged loops in RNase (first column, Fig. 3c). For example, a loop linking ATF7 and KRT18 genes that was absent in Control and NH₄OAc emerged in both FL and RNase (arrows, Fig. 3d, Supplementary Fig. S3).

The overall loop strength was similar in Control and NH₄OAc, but stronger in FL and RNase, as reflected by both Peak to Lower Left (P2LL) (Fig. 3e) and Z-score Lower Left (ZscoreLL) scores⁵ (Fig. 3f). We repeated these analyses based on the union of the loops in the four conditions and quantified every loop's strength by Peak to Mean (P2M) in each condition. P2Ms were greater in FL and RNase than in Control (p -value < 2.2e-16, Wilcoxon test), whereas NH₄OAc's P2Ms were not different from the control's (p -value = 0.41, Wilcoxon test) (Fig. 3g). The consistent increases of loop strengths in FL and RNase as compared to Control support our detected increases of loop numbers in FL and RNase and suggest that our conclusion of loop number increases does not depend on the threshold of loop calls. Taken together, FL and

RNase both resulted in an increase of chromatin loops and these emerged loops often co-localize. As opposed to the null hypothesis that RNA does not have a genome-wide impact on chromatin looping, these data are in favor of a suppressive effect of RNA to chromatin looping genome-wide.

RNA's genomic target regions correlate with the suppressed chromatin loops

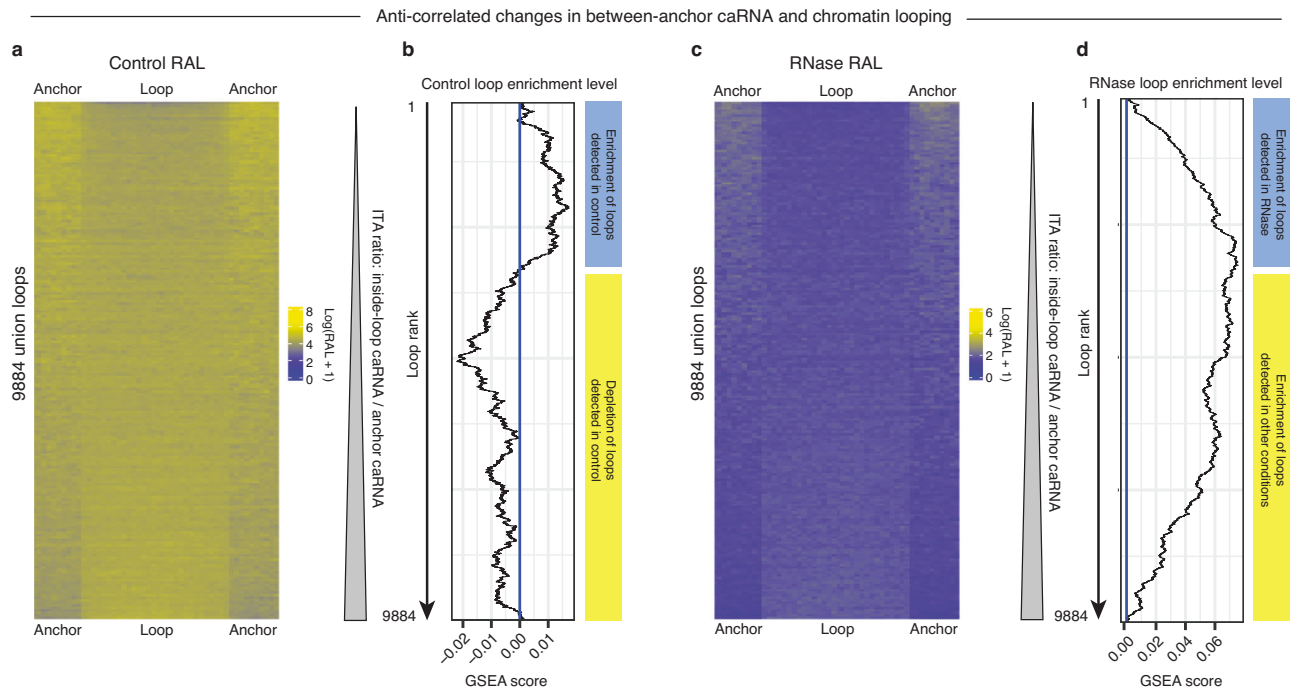
Our next question is what RNA has an impact on which chromatin loops. Although we cannot analyze every aspect of a select RNA, we can analyze the chromatin-associated fraction of this RNA, in terms of this RNA's genomic target regions (target region) and the RNA attachment level (RAL) of this RNA on any target region. We can compare the target region with the genomic location of any chromatin loop. Thus, we asked whether the change of any caRNA, in terms of changes of target regions or RAL, correlates with the change of any chromatin loop. Answering this question can inform us on which RNA could impact which chromatin loop, although we will miss those impacts that are independent of RNA-chromatin association.

We generated iMARGI data in each treatment condition (NH₄OAc, FL, RNase) in duplicates (Table S1) and analyzed these data together with those of the unperturbed H1 cells (control). As expected, FL exhibited the largest reduction of the heights of the rectangular blocks in iMARGI's contact matrix (p -value < 3e-104, Wilcoxon rank-sum test) (Supplementary Fig. S4e), consistent with FL's inhibitory effect on transcription elongation⁴⁸. RNase exhibited the largest reduction of caRNA domains' number (3217 in Control and 357 in RNase, p -value < 3e-9, paired t-test) (Supplementary Fig. S4d) and sizes (widths of the rectangular blocks) (p -value < 5e-210, Wilcoxon rank-sum test) (Supplementary Fig. S4f).

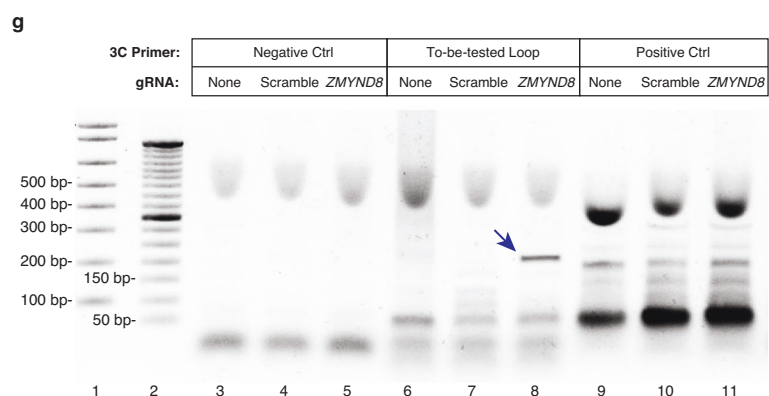
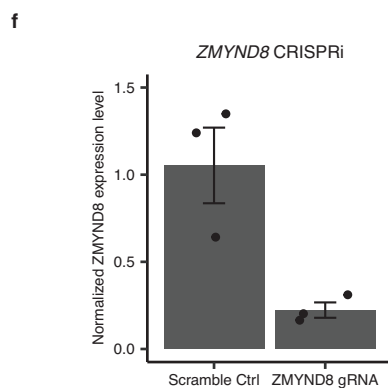
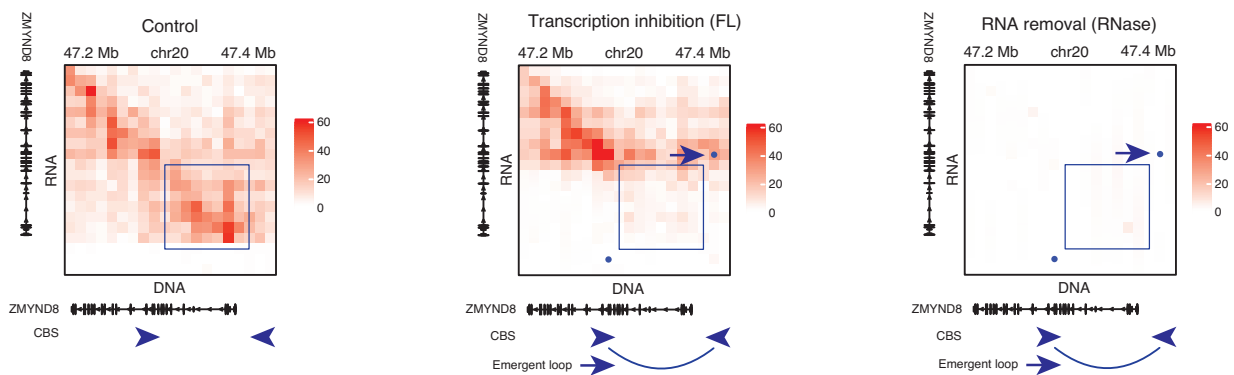
We analyzed two groups of caRNA, namely those associated with loop anchors (anchor caRNA), and those between loop anchors (between-anchor caRNA). We asked if the changes in the level of between-anchor caRNA correlate with the changes of chromatin loops across our treatment conditions. To answer this question, we analyzed the union of the loops (Union loops) detected in every condition (Control, NH₄OAc, FL, RNase). These Union loops represent all possible loop locations, including those detected as loops in Control (control loop) or in an RNA perturbation experiment (emergent loop). We used the ratio of between-anchor caRNA and anchor caRNA levels (Inside-loop To Anchor ratio (ITA ratio)) to represent the relative level of between-anchor caRNA for any Union loop.

First, we tested whether the detected loops in control (control loops) tend to locate at the genomic locations with a low level of between-anchor caRNA in the control. We carried out this test using Gene Set Enrichment Analysis (GSEA)⁶². According to GSEA's procedure, we sorted the Union loops by increasing levels of between-anchor caRNA, i.e., increasing ITA ratios, creating a ranked list (Fig. 4a). We then plotted the corresponding GSEA score at every rank (Fig. 4b), where a positive/negative GSEA score indicates an enrichment/depletion of the control loops in the subset of top-ranked Union Loops. Here, top-ranked means from rank #1 to the current rank on which GSEA score is reported. The GSEA scores stayed positive in the top portion (~30%) of this ranked list (Fig. 4b), suggesting that the control loops are enriched in those Union loops that exhibit lower levels of between-anchor caRNA in the control condition than in the other conditions. In other words, among all the locations where loops have been detected, the control loops tend to appear at those locations where the relative level of between-anchor caRNA is low.

Second, RNase reduced caRNA levels in all Union loops (Fig. 4c) and nearly doubled the number of detected loops as compared to Control (Fig. 3c). We tested whether the loops in RNase (RNase loops) appeared at the locations where the between-anchor caRNA is most rigorously depleted in RNase. To this end, we re-ordered the Union loops by increasing levels of between-anchor caRNA, i.e., the ITA ratio



e Induction of a specific loop by CRISPRi



in RNase (Fig. 4c). As expected, all the GSEA scores are positive in this analysis (Fig. 4d), which is because the RNase loops comprise the majority (~75%) of the Union loops, and therefore a majority in any top ranked subset. The GSEA scores in this ranked list of Union loops first increased and then decreased, which means that the RNase loops are enriched in the higher ranked subset, which are the Union loops with

low levels of between-anchor caRNA in RNase. This enrichment means that the emerged loops in RNase often appeared at the genomic locations where the between-anchor caRNA is most rigorously removed by RNase. Taken together, we observed a genome-wide negative correlation among between-anchor caRNA and the chromatin loops that stride across the target region of these caRNA.

Fig. 4 | Between-anchor caRNA anticorrelates with chromatin looping. **a, b** The loops in Control (control loops) are depleted with between-anchor caRNA. **a** The caRNA levels in the control sample (Control RAL) on loop anchors (two sides) and between the anchors (middle) is color-coded (blue: low, yellow: high) for every loop detected in any condition (Union loops, rows). Loops are ranked by the relative level of their between-anchor caRNA (Inside-loop To Anchor (ITA) ratio) from low (top) to high (bottom). **b** The enrichment/depletion level (GSEA score, x axis) of the control loops in the subset of loops from the top-ranked loop (first row) and the currently ranked loop (current row, y axis). A positive/negative GSEA score indicates an enrichment/depletion of the control loops in this subset of loops. The control loops are enriched in the top-ranked loops, i.e., those with low levels of between-anchor caRNA (blue bar on the right), and are depleted in the bottom-ranked loops, i.e., those with high levels of between-anchor caRNA (yellow bar). **c, d** RNase emergent loops are those with low levels of between-anchor caRNA. **c** The caRNA levels in RNase (RNase RAL) on loop anchors (two sides) and between the anchors (middle) is color-coded (blue: low, yellow: high) for every loop detected in any condition (Union loops, rows). The union loops (rows) are ordered by the relative level of their between-anchor caRNA (the ITA ratio calculated in RNase) from low (top) to high (bottom). **d** The enrichment level (GSEA score, x axis) of the RNase loops (x axis) in the subset of loops from the top-ranked loop (first row) and the currently ranked loop (current row, y axis). The RNase-specific loops are enriched in the top-ranked loops, i.e., the loops with low levels of between-anchor caRNA in RNase, as indicated by the increasing GSEA scores (blue bar on the right). In contrast, the loops detected in other conditions are enriched in the

bottom-ranked loops, i.e., the loops with high levels of between-anchor caRNA in RNase, as indicated by the decreasing GSEA scores (yellow bar). **e–g** Transcriptional suppression of the *ZMYND8* gene induces a specific chromatin loop. **e** Changes in iMARGI RNA-DNA contact maps in Control (left panel), FL (central panel), and RNase (right panel). FL reduced the caRNA in the upstream region of the *ZMYND8* gene (blue box) and induced a chromatin loop near the caRNA-depleted region (curve at the bottom). RNase reduced the caRNA from a wider genomic region and induced the same chromatin loop as that in FL. CBS: CTCF binding sites. Arrowheads point to CBS' directions. Blue dots: Hi-C derived loops that are superimposed on this iMARGI contact map. Arrow: the emergent loop in FL. **f** Comparison of normalized *ZMYND8*'s expression levels (y axis) in CRISPRi experiments with the scrambled gRNA (Scramble Ctrl) and *ZMYND8*-targeting gRNA (*ZMYND8* gRNA). Data are presented as mean values \pm SEM ($n = 3$ replicates). **g** 3 C products from the Negative Ctrl primers (the first 3 lanes), the primers for the To-be-tested loop (3 middle 3 lanes), and the Positive Ctrl primers (the last 3 lanes) in CRISPRi experiments without a gRNA (gRNA: None), with a scrambled gRNA control (gRNA: Scramble), or with the *ZMYND8*-targeting gRNA (gRNA: *ZMYND8*). The Negative Ctrl primers did not yield any product in any experiment (Lanes 3–5). The Positive Ctrl primers yielded products of the same sizes in all three experiments (Lanes 9–11). The primers for the to-be-tested loop yielded a product with *ZMYND8*-targeting gRNA (arrow) but not with a scrambled gRNA or without gRNA (Lanes 6–8), confirming that a loop is created by *ZMYND8* CRISPRi. Lane 1: E-Gel™ 1 kb DNA Ladder. Lanes 2: E-Gel™ 50 bp DNA Ladder. Each experiment was repeated independently 3 times. Source data are provided as a Source Data file.

Reducing select RNA creates specific chromatin loops

We wondered if we could apply the aforementioned correlation to identify which RNA has an impact on what chromatin loops. To this end, we tested whether we could create a particular chromatin loop by reducing a specific RNA, which is the RNA that exhibits a strong level of chromatin attachment to the genomic region between the anchors of this chromatin loop. We chose the *ZMYND8* RNA for this test. We chose the *ZMYND8* RNA because (1) FL reduced the RAL of the *ZMYND8* RNA in an approximately 90 kb genomic region (Fig. 4e); (2) RNase also removed the *ZMYND8* caRNA in this (and a larger) genomic region; (3) a chromatin loop straddling across this 90 kb region was detected by Hi-C in both FL and RNase (arrows, Fig. 4e), hereafter called the “straddling loop”. We note that FL and RNase reduce the RALs of many RNAs, and thus from these data we cannot conclude that the emergence of this straddling loop in FL and RNase is due to the reduction of any specific RNA.

RNA knockdown without affecting transcription can reduce nucleoplasmic RNA and suppress long-range RNA-chromatin interactions, however, it cannot effectively remove nascent RNA that are associated with the chromatin near the transcription locus²¹. Therefore, we do not have a method to effectively remove *ZMYND8* caRNA near the *ZMYND8* gene without affecting the transcription of the *ZMYND8* gene. We employed two approaches to address this issue. First, we asked whether suppression of *ZMYND8* transcription has the same effect as RNase in creating the “straddling loop”. Second, we will describe in subsequent sections the analysis of inter-chromosomal RNA-chromatin interactions, where we can better distinguish between impacts of the RNA from the transcriptional process.

We suppressed *ZMYND8* by CRISPR interference (CRISPRi) in an H1 ES cell line with doxycycline-inducible dCas9-KRAB^{45,63}. Compared to scrambled gRNA control, our gRNA targeting *ZMYND8*'s promoter reduced *ZMYND8*'s transcription level to approximately 25% (Fig. 4f). We designed chromosome conformation capture (3C) primers⁴⁶ for (1) a negative control “loop” (Negative Ctrl) that is located 200 kb upstream of the emerged loop and has approximately the same size as the emerged loop, which is not detected as a loop in any Hi-C experiment, (2) a positive control loop (Positive Ctrl) detected by Hi-C in both Control and FL, which is not on the same chromosome as *ZMYND8*, and (3) the straddling loop (also termed the “to-be-tested loop”). We carried out 3C after treating the cells with doxycycline without supplying gRNA (gRNA:None Ctrl), supplying with a scrambled

gRNA (gRNA:Scramble Ctrl), and with gRNA targeting *ZMYND8*'s promoter (gRNA:*ZMYND8*). The Negative Ctrl primers did not yield any product in any experiment (the first 3 lanes), and the Positive Ctrl primers yielded products at the expected sizes in all three experiments (the last 3 lanes, Fig. 4g). In contrast, the primers for the to-be-tested loop yielded a unique product with *ZMYND8* gRNA (arrow, Fig. 4g), which is absent from the gRNA:None and gRNA:Scramble controls. In summary, acute reduction of RNA induced many chromatin loops including the straddling loop, and suppression of the *ZMYND8* expression can re-create the emergence of the straddling loop. Thus, the negative correlation of between-anchor caRNA and chromatin loops can help to identify which RNA has an impact on which chromatin loop. We note that the CRISPRi experiment by itself cannot distinguish whether the loop was created by suppression of transcription or reduction of *ZMYND8* RNA. This CRISPRi experiment demonstrates that a loop created by acute depletion of RNA (RNase) can be re-created by suppression of the expression of a specific gene.

Acute RNA reduction increases the average strength of the loops with convergent CTCF binding sites in their loop anchors

Our next question is whether an RNA can impact the chromatin loops located far from the transcription locus of this RNA (distal loops). We recognize that our previously mentioned correlation is not sufficient to connect a specific RNA to specific distal loops. This is because an RNA can associate with many distal genomic regions, often at low levels. Thus, we proceeded to identify additional correlational rule(s) between RNA and chromatin loops.

Convergent CTCF binding sites (CBS) in the loop anchors is a characteristic of the loops created by loop extrusion⁶⁰. We tested whether the convergent CBS are enriched in the anchors of the loops with increased loop strengths in RNase. To this end, we categorized the Union Loops (the union of the loops detected in any treatment condition) into three groups based on the orientations of the CTCF binding sites at their anchors, namely the loops with convergent CBS, non-convergent CBS, or no CBS. We used Peak to Lower Left (P2LL) to quantify the strength of each loop⁵. Compared to Control, RNase treatment increased P2LL in the Union Loops with convergent CBS (p -value $< 1.6E-9$, Wilcoxon test, Fig. 5a). In comparison, RNase did not increase P2LL in the Union Loops with non-convergent CBS (p -value = 0.4663, Wilcoxon test, Fig. 5a) or in the loops without CBS (p -value = 0.6277, Wilcoxon test, Fig. 5a). Thus, acute RNA reduction

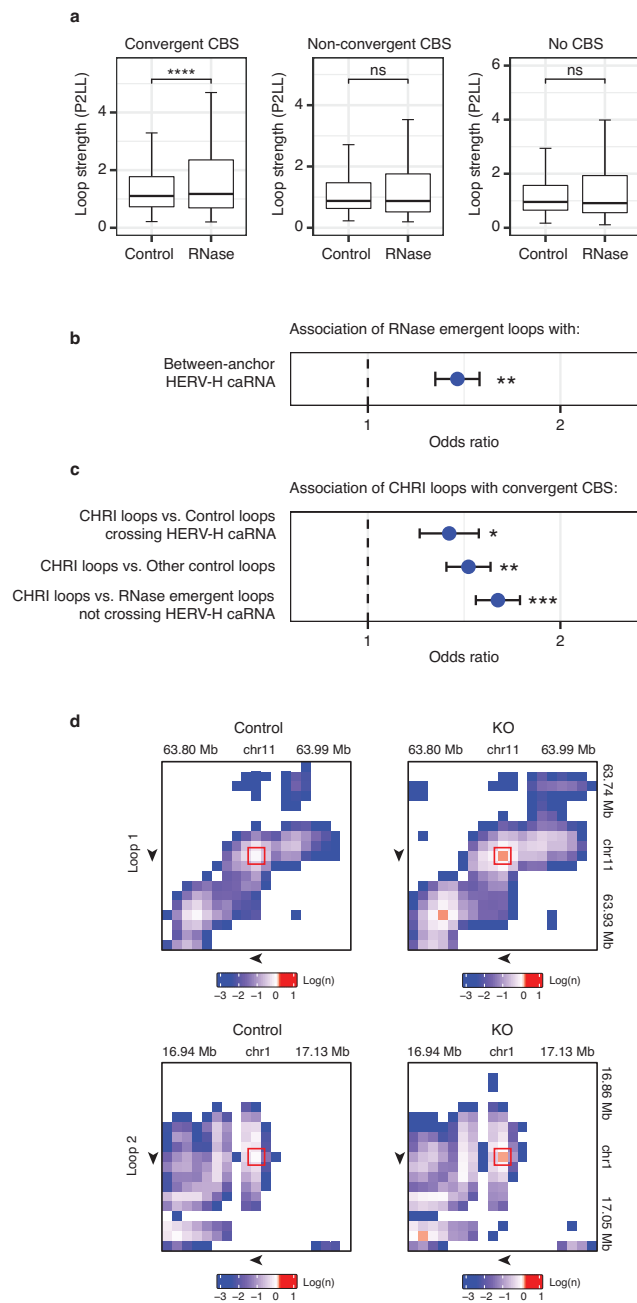


Fig. 5 | Enrichment of convergent CTCF binding sites (CBS) in the anchors of RNA-affected loops. **a** Comparison of loop strengths (P2LL, y axis) in the loops with convergent CBS, non-convergent CBS, and without CBS in Control and RNase (columns). **** p -value = $1.571e-9$. ns: not significant (p -values = 0.466 and 0.628 for Non-convergent CBS and No CBS respectively), Wilcoxon test. The center line of the boxplots is the median. The lower and upper hinges correspond to the first and third quartiles (the 25th and 75th percentiles). The upper whisker extends from the hinge to the largest value no further than $1.5 \times$ IQR from the hinge (where IQR is the inter-quartile range, or distance between the first and third quartiles). The lower whisker extends from the hinge to the smallest value at most $1.5 \times$ IQR of the hinge. **b** Enrichment of RNase emergent loops with between-anchor HERV-H caRNA in Control (odds ratio, x axis). ** p -value = $5.621e-5$, Chi-square test ($n = 8112$ chromatin loops). Odds ratio > 1 means enrichment. Data are presented as odds ratios, with the error bar whiskers at $\exp(\log(\text{OR}) \pm \text{SELOG})$, where SELOG is the standard error of the log odds ratio. **c** Enrichment of “candidate HERV-H caRNA insulated loops” (CHRI-loops) with convergent CBS in their loop anchors as compared to control loops striding across HERV-H caRNA-attached genomic sequences (first row, $n = 1653$ chromatin loops), the other control loops not striding across HERV-H caRNA-attached genomic sequences (second row, $n = 4059$ chromatin loops), and the RNase emergent loops not striding across any HERV-H caRNA-attached genomic sequences (third row, $n = 4219$ chromatin loops). * $p = 6.884e-3$, ** $p = 5.857e-6$, *** $p < 4.056e-9$, Chi-square test. Data are presented as odds ratios, with the error bar whiskers at $\exp(\log(\text{OR}) \pm \text{SELOG})$, where SELOG is the standard error of the log odds ratio. **d** The two target-crossing loops (rows) with increased Hi-C contacts in HERV-H KO (KO column) as compared to Control (Control column). Hi-C data were denoised using the DeepLoop software. The denoised Hi-C contact maps were shown in the log scale. Arrow: direction of CTCF binding site in the loop anchor. Source data are provided as a Source Data file.

increased the average strength of those loops with convergent CBS in their loop anchors, suggesting an enrichment of convergent CBS in anchors of RNA suppressed loops. In summary, we have observed two genome-wide correlations, which are (1) a negative correlation of between-anchor caRNA and chromatin loops and (2) an enrichment of convergent CBS in RNA suppressed loops. Hereafter we call these correlations the “correlational rules”.

Removal of select RNA increases the strengths of a subset of distal chromatin loops

We wondered if we could apply the aforementioned correlational rules to identify which RNA may have an impact on what distal chromatin loops. To this end, we tested whether removing specific RNA can increase the strengths of certain distal loops. We chose the HERV-H RNA for this test for the following reasons. First, we identified the HERV-H caRNA-associated genomic sequences (HERV-RNA target regions) in Control and compared them with the locations of the loops emerged in RNase (RNase emergent loops). The RNase emergent loops

are enriched at the locations that exhibit between-anchor HERV-H caRNA in Control (odds ratio = 1.38, p -value = $5.621e-5$, Chi-square test, Fig. 5b), suggesting that those loops that stride across between-anchor HERV-H caRNA are suppressed in Control. Second, we analyzed the subset of RNase emergent loops that stride across HERV-H caRNA-attached genomic sequences in Control. Hereafter, we call this subset of RNase emergent loops as “candidate HERV-H caRNA insulated loops” (CHRI-loops). CHRI-loops are enriched with convergent CBS in their loop anchors as compared to (1) control loops striding across HERV-H caRNA-attached genomic sequences (OR = 1.34, $p = 0.0068$, Chi-square test), and to (2) the other control loops not striding across HERV-H caRNA-attached genomic sequences (OR = 1.44, $p = 5.8e-6$, Chi-square test), and to (3) the RNase emergent loops not striding across any HERV-H caRNA-attached genomic sequences in Control (OR = 1.60, $p = 4.1e-9$, Chi-square test, Fig. 5c). Thus, convergent CBS are enriched in the loop anchors of CHRI-loops.

We tested whether deleting an HERV-H element from the human genome can lead to increasing the loop strength of any distal CHRI-loop. To this end, we re-used our Chr13:55.5MB_HERV KO (CRISPR-mediated deletion of a HERV-H element at Chr13:55,578,227-55,584,087) human ES cells⁴². We identified the caRNA transcribed from this Chr13:55.5MB_HERV element and its target genomic sequences (Chr13:55.5MB_HERV targets) in the WT. We call the loops that stride across any Chr13:55.5MB_HERV targets as “target-crossing loops”. We compared the loop strength changes of all target-crossing loops between Chr13:55.5MB_HERV KO and WT based on Hi-C data. No target-crossing loop exhibited detectable decrease in loop strength in Chr13:55.5MB_HERV KO, whereas two target-crossing loops exhibited increased loop strengths in the Chr13:55.5MB_HERV KO (Fig. 5d). Both Chr13:55.5MB_HERV KO-induced target-crossing loops contain convergent CBS in their loop anchors (Fig. 5d). Neither Chr13:55.5MB_HERV KO-induced target-crossing loop locates on Chromosome 13, where the HERV-H element is deleted (Fig. 5d). Thus, removal of specific RNA increased the loop strengths of a subset of chromatin loops that stride across this RNA’s interchromosomal target regions and contain convergent CBS in their loop anchors. These data suggest specific RNA modulate a subset of chromatin loops.

Furthermore, the correlational rules help to identify which RNA modulates what chromatin loops.

Discussion

We presented a resource composed of genome-wide RNA-DNA and DNA-DNA contact maps in three human cell lines. The iMARGI and Hi-C experimental protocols and data processing pipelines used for generating this resource were proven by the 4D Nucleome (4DN) Consortium Omics Standards Working Group and the 4DN Steering Committee (<https://www.4dnucleome.org/protocols/>). The three human cell lines for data generation were nominated by the 4DN Joint Analysis Working Group and cultured under the 4DN Cell Working Group approved protocols (<https://www.4dnucleome.org/cell-lines/>). All the data are accessible through the 4DN Data Portal (see Data Availability and Table S1).

The initial challenges to caRNA as a distinct class of RNA were focused on whether these RNAs are exclusively nascent transcripts⁹. Such a concern was alleviated by the discoveries of long-range RNA-chromatin interactions^{10–14}, suggesting that caRNA does not completely overlap with nascent transcripts. Our genome-wide analyses reveal two features of RNA-genome association. First, RNA is preferentially associated with its transcription site and up to several megabases of flanking genomic sequence. Second, TAD boundaries insulate RNA-DNA contacts, evidencing the impact of 3D genome on the spatial distribution of caRNA.

It remains unclear how RNA may affect the 3D genome. Because several 3D features of the genome can be reproduced by computational models without considering RNA^{64,65} and in vitro experiments to recapitulate loop extrusion without RNA⁶⁶, RNA was not expected to affect the genome's 3D organization. Furthermore, previous work found that acute reduction of RNA had subtle impacts to the 3D genome at the compartment and the TAD levels⁵⁰. Our analyses led to similar findings. At the compartment level, Hi-C's PCI in FL and RNase exhibited strong correlations with Hi-C's PCI in Control, suggesting these perturbations had little impact to A/B compartments. At the TAD level, FL and RNase exhibited “highly concordant” TADs with the control, based on the “Measure of Concordance (MoC)”⁶⁴ (pairwise MoCs = 0.93 and 0.90, well above 0.75, the threshold for being “highly concordant”⁶⁴). These data confirm that the impacts of RNA to the 3D genome are subtle, at least at the scales of A/B compartments and TADs.

It has not been tested whether an acute reduction of RNA exerts systematic impacts to chromatin loops. Our data reveal either transcription inhibition or acute RNA reduction induced chromatin loops. Most induced loops are shared between transcription inhibition and acute RNA reduction, indicating that the impact on chromatin looping cannot be completely attributed to transcription or the presence of RNAPII on chromatin. Indeed, suppressing a specific caRNA created a chromatin loop, with the loop anchors striding across the genomic sequence associated with this caRNA (Fig. 4e–g). Furthermore, deleting the genomic sequence of a caRNA (Chr13:55.5MB_HERV) strengthened the chromatin loops on other chromosomes (Fig. 5d). These inter-chromosomal effects argue against that loop strengths are modulated by the transcription of the deleted sequence. They support the idea that the caRNA at specific locations, i.e. between-anchor caRNA, suppresses chromatin looping. Of note, these experiments were not meant to establish an exclusive role of RNA in modulating chromatin looping. While these data establish RNA's role, they do not exclude transcription or RNAPII's role in modulating chromatin looping.

What remains to be addressed is whether there is any rule that links specific RNA with specific loops that this RNA can modulate. Disrupting electrostatic interactions by NH₄OAc did not lead to significant changes in chromatin loops, withholding us from exploring possible rules based on charge-mediated condensates or phase

separation. Instead, we investigated RNA's target regions, because the genomic locations of the target regions can be compared with the genomic locations of loops. We found the caRNA located between the two anchors of a chromatin loop often weakens this loop. This suppressive role of between-anchor caRNAs is compatible with the recently reported promotive role of the caRNAs with complementary sequences to chromatin looping^{65,66}. When two caRNAs, that are attached to two genomic sequences, have complementary sequences, they tend to bring their associated genomic sequences to spatial proximity, thus promoting loop formation⁶⁵. Following the same idea, any sequence complementarity between any between-anchor caRNA and any other caRNA associated with any outside-of-loop genomic sequences could promote spatial proximity of this between-anchor genomic sequence and those outside-of-loop genomic sequences, thus reducing the spatial proximity of the loop anchors. Thus, a unified model can explain the suppressive role of between-anchor caRNA and the promotive role of the caRNAs with sequence complementarity on chromatin looping.

Recent work revealed a suppressive role of RNAPII's presence on chromatin to chromatin looping⁴³. Without underestimating RNAPII's role, our experiments were designed to test if there are any effects of the RNA as well. FL treatment does not displace RNAPII from chromatin⁵⁴, making the FL emergent loops unlikely due to a change of RNAPII's presence on chromatin. Furthermore, our analysis focused on the shared loops that are created by both FL or RNase treatment. These shared loops are even more unlikely attributable to the loading of RNAPII on chromatin. Our data suggest that in addition to RNAPII, RNA should be considered toward obtaining a complete picture on the interplay between transcription and genome organization.

Methods

Cell culture and treatments

Human embryonic stem cells (H1), hTert-immortalized human foreskin fibroblasts (HFF), and chronic myelogenous leukemia lymphoblasts (K562) were obtained from the 4D Nucleome (4DN) Cell Repository and cultured following the 4DN Consortium's approved culture protocol for each cell line (<https://www.4dnucleome.org/cell-lines.html>). The cell lines in the 4DN Cell Repository were established by the 4DN Consortium in collaboration with WiCell and ATCC for providing quality-controlled cells from the identical batch to minimize cell source and culture condition variations. The cell culture protocols were developed by the 4DN Cell Line Working Group and approved by the 4DN Steering Committee.

Ammonium acetate treatment. H1 cells were treated with 0.1M NH₄OAc in complete mTeSR medium for 10 min as described in a previous study⁵². Briefly, a crystalline NH₄OAc (Sigma-Aldrich, Cat# A1542-500G) was dissolved in nuclease-free water and further diluted in cell medium. Aspirate medium in each well and H1 cells were treated with 0.1 M NH₄OAc in medium for 10 min at RT.

Flavopiridol treatment. H1 cells were treated with 1 μM flavopiridol in complete mTeSR medium for 1 h in an incubator as described previously⁴⁸. Specifically, a crystalline flavopiridol (hydrochloride) (Cayman Chemical, item# 10009197) was dissolved in DMSO to prepare 1 mM flavopiridol (FL) stock solution. 1 mM FL stock solution was further diluted with complete mTeSR medium. Aspirate cell medium in each well and H1 cells were either treated with 1 μM FL in medium or an equivalent amount of DMSO in the medium in an incubator at 37 °C for 1 h.

RNase A treatment. H1 cells were harvested from cell culture plate and aliquoted cell suspension to 10 million H1 cells per 1.5 mL tube. Wash the cells with 1 mL 1X PBS and centrifuge at 500 X g for 3 min at RT. Then, cells were gently permeabilized by resuspending cell pallets with

0.01% PBST (TritonX-100 in PBS) and treated for 5 min at RT. After permeabilization, cells were treated with 200 µg/mL RNase A as described previously⁵⁰ (Thermo Fisher Scientific, Cat# EN0531) on rotator for 10 min at RT. The treated cells were fixed with 4% formaldehyde (Thermo Fisher Scientific, Cat# 28906) for immunofluorescence imaging. For Hi-C and iMARGI library generation, the treated cells were fixed with 1 mL 1% formaldehyde on rotator for 10 min at RT. Then, the reactions were terminated with 250 µL 1 M glycine on rotator for 10 min at RT. The treated sample was centrifuged at 2000 X g for 5 min at 4 °C and washed with 1 mL cold 1X PBS.

dCas9-KRAB inducible cells. The doxycycline-inducible dCas9-KRAB H1 ES cell line is generated and karyotyped by the 4D Nucleome Consortium (Danwei Huangfu Laboratory) (<https://4dnucleome.org>), with TRE-dCas9-KRAB and CAGGS-M2rtTA targeted into the AAVS1 locus.

HERV-H deletion and insertion cells. The control H9 human ES cells (H9 MLC2v:H2B), HERV-H deletion cell line (H9 MLC2v:H2B HERV2-KO), and HERV-H insertion cell line (H9 MLC2v:H2B HERV2-ins-clone2) were generated by Bing Ren lab and described in ref. 42.

RPB1 The auxin-inducible degron 2 cells. The RPB1 auxin-inducible degron 2 cells (HCT116 RPB1-Dox-OsTIR1-mClover-mAID) were generated by Masato Kanemaki lab and described in ref. 67.

Calling de novo TAD boundaries

TAD boundaries in WT (H9 MLC2v:H2B) and KI (H9 MLC2v:H2B HERV2-ins-clone2) were separately called based on their respective Hi-C data using The Arrowhead tool in the Juicer Tools⁶¹ with default parameters. A TAD boundary called in KI but not in WT is regarded as a de novo TAD boundary.

Immunofluorescence imaging

The cells on coverslip (Fisher Scientific, Cat# 12-541 A) were fixed with 4% formaldehyde at RT for 30 min. The fixed cells were washed with 1X PBS once and permeabilized with 0.1% TritonX-100 in PBS (PBST) at RT for 15 min on shaker. Afterwards, cells were blocked with 5% BSA (VWR, Cat# 97061-420) in PBST at RT for 30 min with gentle shaking. For SC35 staining, HI cells were incubated with 1 mL diluted mouse monoclonal anti-SC35 primary antibody (1:250) (Abcam, Cat# ab11826) in 5% BSA at 37 °C for 1 h, and subsequently washed three times with PBST on shaker for 10 min. Cells were further incubated with 1 mL diluted goat anti-mouse secondary antibody with Alexa Fluor 568 (1:500 dilution) (Invitrogen, Cat# A-11004) in 5% BSA at 37 °C for 30 min. For SON staining, the cells were incubated with 1 mL diluted rabbit anti-SON primary antibody (1:2000 dilution) (Atlas Antibodies, HPA023535) in 5% BSA at 37 °C for 1 h, and subsequently washed three times with PBST on shaker for 10 min. The cells were incubated with 1 mL diluted goat anti-rabbit secondary antibody with Alexa Fluor 488 (1:500 dilution) (Invitrogen, Cat# A-11008) in 5% BSA at 37 in 5% BSA at 37 °C for 30 min. After staining, the cells were washed three times with PBST on shaker for 10 min. The cells on coverslips were mounted on slides (Fisher Scientific, Cat# 12-544-2) with 10 µL ProLong antifade glass mountant with NucBlue stain (Thermo Fisher Scientific, Cat# P36981), placed in dark room for air-dry overnight. Images in the size of 512 × 512 pixels were acquired on Applied Precision OMX Super Resolution Microscope using a 100X/1.518 oil objective (GE Healthcare Life Sciences) (pixel size = 0.079 µm). Z-stack images were acquired with a 0.3 µm sample thickness.

Identification of nuclear speckle foci

Nuclear speckle foci were identified by a previously described method⁴⁸. Briefly, the nuclei were manually segmented and the mean

fluorescence intensity in nuclei was measured with FIJI. The nuclear speckle foci were identified by FIJI 3D Object Counter plugin, with an appropriate intensity threshold of the mean fluorescence intensity in the cell nuclei and a size cut-off of more than 50 adjoining pixels (pixel size, 79 nm X 79 nm).

In situ Hi-C library generation and data processing

The Hi-C libraries were generated with the Arima-HiC kit (Arima Genomics, material# A510008, Document# A160134 v00) following the manufacturer's instructions and processed following 4DN consortium's in situ Hi-C processing protocol (<https://www.4dnucleome.org/protocols.html>). Next, the Hi-C data were processed using the 4D Nucleome (4DN)'s Hi-C data Processing Pipeline (v0.2.5) (https://data.4dnucleome.org/resources/data-analysis/hi_c-processing-pipeline), with MAPQ > 30 to filter out multiple mappings.

The output .pairs files were provided to Cooler⁶⁸ (v0.8.10) and Juicer Tools⁶¹ (v1.22.01) to generate .mcool and .hic files. The .mcool file was used in HiGlass⁶⁹ for visualization. The .hic files were inputted in Juicer Tools for A/B compartment, TAD, and loop analyses. A/B compartments were called by Juicer's "Eigenvector" tool based on KR normalized observed/expected (O/E) contacts at 500 kb resolution. TADs were called by Juicer's "Arrowhead" tool based on KR-normalized contacts at 10 kb resolution. Loops were called by Juicer's "CPU Hi-CUPS" tool based on KR-normalized contacts simultaneously at 5 kb and 10 kb resolutions. Except for the resolution parameter, all the other parameters were left as the default.

TAD boundaries were extracted as the genomic regions between TADs in each sample. TAD boundary insulation score was calculated according to the definition in Crane et al.⁷⁰.

Unique loops and overlapping loops were determined as follows. First, the Juicer called loops from each condition were merged into "unique loops" by taking the union. Then the unique loops in the union were reassigned to each condition by the following rule: a unique loop *i* (in the union) with anchor size *s* (either 5 or 10 kb) was re-assigned to a sample *j* if both anchors of loop *i* were within +/-*s* flanking regions of a loop in sample *j*. Aggregate Peak Analysis was performed using the Juicer's "APA" tool with default parameters. Metrics to define the loop strength such as Peak to Lower Left (P2LL), Z-score Lower Left (ZscoreLL), and Peak to Mean (P2M) were calculated as defined in Juicer's APA⁶¹. The control loop straddling the AAVS1 locus was detected from HI-hESC Micro-C data⁴⁴. To select RNase emergent loops that stride across HERV-H caRNA-attached genomic sequences in Control, i.e., the candidate HERV-H caRNA insulated loops (CHRI-loops), we used a threshold of at least 2 iMARGI read pairs with their RNA ends overlapping with HERV-H and their DNA ends mapped to the between-loop-anchor sequence. To check if deleting a copy of the HERV-H repeats led to increase of loop strengths of CHRI-loops, we used a threshold of 0.05 for the delta peak (KO peak - control peak), where peak is the normalized Hi-C read count at the loop's pixel, normalized by the total number of read pairs in each sample.

Production of gRNAs through in vitro transcription (IVT)

gRNA was synthesized by assembly PCR and in vitro transcription as previously described in ref. 71. Briefly, a T7 RNA polymerase substrate template was assembled by PCR from a variable 58–59 nt primer containing T7 promoter, variable gRNA guide sequence, the first 15 nt of the non-variable region of the gRNA (T7FwdVar primers, 10 nM), and an 83 nt primer containing the reverse complement of the invariant region of the gRNA (T7RevLong, 10 nM), along with amplification primers (T7FwdAmp, T7RevAmp, 200 nM each). The two long primers anneal in the first cycle of PCR and are then amplified in subsequent cycles. Phusion high-fidelity DNA polymerase was used for assembly (New England Biolabs). Assembled template was used without purification as a substrate for in vitro transcription by T7 RNA polymerase, using the HiScribe T7 High Yield RNA Synthesis kit (New England

Biolabs-E2040S) following the manufacturer's instructions. Resulting transcription reactions were treated with DNase I (New England Biolabs-M0303S), and RNA was purified by Qiagen RNeasy mini spin column (Qiagen-74104) and eluted in RNase-free water.

Phosphatase treatment of IVT gRNAs

gRNAs were treated with phosphatases as follows: rSAP (New England Biolabs-M0371S) were added per 20 μ l in vitro transcription reaction, and samples were incubated at 37 °C for 3 h before proceeding to purification and DNaseI treatment. gRNA was purified using a Qiagen RNeasy Mini Kit (Qiagen-74104). The detailed protocol and additional notes are available online (<https://doi.org/10.17504/protocols.io.nghdbt6>).

gRNA Transfection

dCas9-KRAB hPSCs were treated with doxycycline (2 μ g/ml) for 24 h before and during transfection. For transfection, cells were dissociated using Accutase (Stem Cell Technologies), replated onto Matrigel (Corning)-coated plates and transfected in suspension with gRNAs using Lipofectamine RNAiMAX (Invitrogen-13778075) following manufacturer's instructions. Briefly, gRNA (mix of 3 guides against ZMYND8) were added at a 10 nM and 20 nM final concentrations respectively, unless otherwise indicated. gRNAs and Lipofectamine RNAiMAX were diluted separately in Opti-MEM (Gibco-31985062), mixed together, incubated for 5 min at RT, and added dropwise to cultured hPSCs. A second transfection was performed 24 hours later in some experiments. Cells were harvested after 2 days.

Generation of 3 C libraries

3 C libraries were generated as previously described in refs. 46,72,73. In brief, 10 million cells were crosslinked with 2% Formaldehyde (Thermo Scientific-28908). Chromatin was digested with DpnII (NEB- R0543T), ligated with T4 DNA ligase (NEB-M0202S) and reverse crosslinked by incubation with Proteinase K (Thermo Scientific-E00491). DNA libraries were purified by phenol/chloroform (Sigma-77617) and subsequent ammonium acetate precipitation (Invitrogen-AM9740). 3 C libraries generated post CRISPRi are used as templates for downstream PCRs.

Bias correction on Hi-C data for loop visualization

H9 Control and HERV-H2 KO Hi-C data were subjected to HiCorr⁷⁴ with default parameters for bias correction and subsequently subjected to noise removal using the LoopDenoise function in DeepLoop⁷⁵. All data processing was done with Hg19 per HiCorr and DeepLoop software's requirements.

iMARGI library generation and data processing

iMARGI libraries were generated and processed as previously described in ref. 36. According to 4DN's approved iMARGI's data processing protocol³⁶, any iMARGI read pair in which the RNA end and the DNA end mapped to within 1000 bp of each other on the genome are removed from the data analysis. The RNA attachment level (RAL) of each genomic segment is the count of the DNA-ends mapped to this genomic segment³⁵. Only the inter-chromosomal and the intra-chromosomal iMARGI read pairs that are separated by at least 200 kb apart were used for calculating RAL in any of the correlation analyses. Repeats of hg38 were downloaded from RepeatMasker (Smit, AFA, Hubley, R & Green, P. RepeatMasker Open-4.0). RAL of Alu-containing caRNA (Alu-caRNA) and LINE1-containing caRNA (LI-caRNA) were calculated as the count of the DNA ends mapped to each genomic segment (500 kb size) whose RNA ends mapped to a repeat segment of the Alu or LINE1 family respectively.

RNA-defined domains

Each rectangular block on iMARGI's contact matrix was identified as a peak of the iMARGI's read pairs' RNA ends (the height of this RNA peak)

and a corresponding DNA peak of the DNA ends (the width of this RNA peak). HOMER's findPeaks⁴⁰ function was applied to the RNA ends of iMARGI' read pairs (peak size = 5000 bp, minimum peak interval = 12,000 bp) to identify the peaks on the RNA ends (RNA peak). For each RNA peak, all the iMARGI's read pairs with their RNA ends inside this RNA peak were retrieved. The retrieved read pairs' DNA ends were subjected to HOMER's findPeaks (peak size = 25,000 bp, minimum peak interval = 50,000 bp) to identify the peaks on the DNA ends (DNA peaks). If multiple DNA peaks were reported, the DNA peak with the highest read number was designated as the corresponding DNA peak.

Genome coordinates

All plotted genome coordinates are based on Hg38.

Primer sequences

See Supplementary Data 1.

Reporting summary

Further information on research design is available in the Nature Portfolio Reporting Summary linked to this article.

Data availability

All high-throughput data supporting the current study have been deposited on the 4D Nucleome Data Portal (<https://data.4dnucleome.org>) with the following IDs. iMARGI datasets: H1 control, 4DNES-NOJ7HY7; H1 NH4OAc, 4DNESGRI8A8N; H1 FL, 4DNES8B3R3P8; H1 RNase, 4DNESOBRUQ12; HFF, 4DNES9Y1GHK4; K562, 4DNESIKCVASO. Hi-C datasets: H1 control, 4DNESFSCP5L8; H1 NH4OAc, 4DNES2253IBO; H1 FL, 4DNES6513RQG; H1 RNase, 4DNES4AABNEZ; HFF, 4DNESNMAAN97; K562, 4DNESI7DEJTM. Source data are provided with this paper.

Code availability

The codes used for the analysis have been deposited and made publicly available on GitHub at <https://github.com/Zhong-Lab-UCSD/RNA3Dgenome-code-repository>.

References

- Dekker, J. et al. The 4D nucleome project. *Nature* **549**, 219–226 (2017).
- Lieberman-Aiden, E. et al. Comprehensive mapping of long-range interactions reveals folding principles of the human genome. *Science* **326**, 289–293 (2009).
- Dixon, J. R. et al. Topological domains in mammalian genomes identified by analysis of chromatin interactions. *Nature* **485**, 376–380 (2012).
- Nora, E. P. et al. Spatial partitioning of the regulatory landscape of the X-inactivation centre. *Nature* **485**, 381–385 (2012).
- Rao, S. S. et al. A 3D map of the human genome at kilobase resolution reveals principles of chromatin looping. *Cell* **159**, 1665–1680 (2014).
- Sun, J. H. et al. Disease-associated short tandem repeats co-localize with chromatin domain boundaries. *Cell* **175**, 224–238.e215 (2018).
- Lupianez, D. G. et al. Disruptions of topological chromatin domains cause pathogenic rewiring of gene-enhancer interactions. *Cell* **161**, 1012–1025 (2015).
- Rao, S. S. P. et al. Cohesin loss eliminates all loop domains. *Cell* **171**, 305–320.e324 (2017).
- Holmes, D. S., Mayfield, J. E., Sander, G. & Bonner, J. Chromosomal RNA: its properties. *Science* **177**, 72–74 (1972).
- Rodriguez-Campos, A. & Azorin, F. RNA is an integral component of chromatin that contributes to its structural organization. *PLoS One* **2**, e1182 (2007).

11. Hall, L. L. & Lawrence, J. B. RNA as a fundamental component of interphase chromosomes: could repeats prove key? *Curr. Opin. Genet. Dev.* **37**, 137–147 (2016).
12. Nozawa, R. S. & Gilbert, N. RNA: nuclear glue for folding the genome. *Trends Cell Biol.* **29**, 201–211 (2019).
13. Nozawa, R. S. et al. SAF-A regulates interphase chromosome structure through oligomerization with chromatin-associated RNAs. *Cell* **169**, 1214–1227.e1218 (2017).
14. Pederson, T. Half a century of locating DNA and RNA in cells. *FASEB J* **33**, 8693–8694 (2019).
15. Li, X. et al. GRID-seq reveals the global RNA-chromatin interactome. *Nat Biotechnol* **35**, 940–950 (2017).
16. Miao, Y. et al. Enhancer-associated long non-coding RNA LEENE regulates endothelial nitric oxide synthase and endothelial function. *Nat. Commun.* **9**, 292 (2018).
17. Place, R. F., Li, L. C., Pookot, D., Noonan, E. J. & Dahiya, R. MicroRNA-373 induces expression of genes with complementary promoter sequences. *Proc. Natl. Acad. Sci. USA.* **105**, 1608–1613 (2008).
18. Morris, K. V., Chan, S. W., Jacobsen, S. E. & Looney, D. J. Small interfering RNA-induced transcriptional gene silencing in human cells. *Science* **305**, 1289–1292 (2004).
19. Penny, G. D., Kay, G. F., Sheardown, S. A., Rastan, S. & Brockdorff, N. Requirement for Xist in X chromosome inactivation. *Nature* **379**, 131–137 (1996).
20. Yang, F. et al. The lncRNA Firre anchors the inactive X chromosome to the nucleolus by binding CTCF and maintains H3K27me3 methylation. *Genome Biol.* **16**, 52 (2015).
21. Calandrelli, R. et al. Stress-induced RNA-chromatin interactions promote endothelial dysfunction. *Nat. Commun.* **11**, 5211 (2020).
22. Watanabe, T. et al. Role for piRNAs and noncoding RNA in de novo DNA methylation of the imprinted mouse Rasgrf1 locus. *Science* **332**, 848–852 (2011).
23. Rinn, J. L. et al. Functional demarcation of active and silent chromatin domains in human HOX loci by noncoding RNAs. *Cell* **129**, 1311–1323 (2007).
24. Xiao, R. et al. Pervasive Chromatin-RNA Binding Protein Interactions Enable RNA-Based Regulation of Transcription. *Cell* **178**, 107–121.e118 (2019).
25. Dumelie, J. G. & Jaffrey, S. R. Defining the location of promoter-associated R-loops at near-nucleotide resolution using bisDRIP-seq. *Elife* **6** <https://doi.org/10.7554/eLife.28306> (2017).
26. Yan, Z. et al. Genome-wide colocalization of RNA-DNA interactions and fusion RNA pairs. *Proc. Natl. Acad. Sci. USA.* **116**, 3328–3337 (2019).
27. Yin, Y. et al. U1 snRNP regulates chromatin retention of noncoding RNAs. *Nature* **580**, 147–150 (2020).
28. Percharde, M. et al. A LINE1-Nucleolin partnership regulates early development and ESC identity. *Cell* **174**, 391–405.e319 (2018).
29. Chen, W. et al. RNAs as Proximity-labeling media for identifying nuclear speckle positions relative to the genome. *iScience* **4**, 204–215 (2018).
30. Quinodoz, S. A. et al. RNA promotes the formation of spatial compartments in the nucleus. *Cell* **184**, 5775–5790.e5730 (2021).
31. Chu, H. P. et al. TERRA RNA Antagonizes ATRX and protects telomeres. *Cell* **170**, 86–101.e116 (2017).
32. Yamazaki, T. et al. Functional Domains of NEAT1 Architectural lncRNA induce paraspeckle assembly through phase separation. *Mol Cell* **70**, 1038–1053.e1037 (2018).
33. Rinn, J. L. & Chang, H. Y. Genome regulation by long noncoding RNAs. *Annu. Rev. Biochem.* **81**, 145–166 (2012).
34. Lee, J. T. Gracefully ageing at 50, X-chromosome inactivation becomes a paradigm for RNA and chromatin control. *Nat. Rev. Mol. Cell Biol.* **12**, 815–826 (2011).
35. Sridhar, B. et al. Systematic Mapping of RNA-Chromatin Interactions In Vivo. *Curr. Biol.* **27**, 602–609 (2017).
36. Wu, W. et al. Mapping RNA-chromatin interactions by sequencing with iMARGI. *Nat. Protoc.* **14**, 3243–3272 (2019).
37. Bell, J. C. et al. Chromatin-associated RNA sequencing (ChAR-seq) maps genome-wide RNA-to-DNA contacts. *Elife* **7** <https://doi.org/10.7554/eLife.27024> (2018).
38. Bonetti, A. et al. RADICL-seq identifies general and cell type-specific principles of genome-wide RNA-chromatin interactions. *Nat Commun* **11**, 1018 (2020).
39. Akgol Oksuz, B. et al. Systematic evaluation of chromosome conformation capture assays. *Nat. Methods* **18**, 1046–1055 (2021).
40. Heinz, S. et al. Simple combinations of lineage-determining transcription factors prime cis-regulatory elements required for macrophage and B cell identities. *Mol. Cell* **38**, 576–589 (2010).
41. Mourad, R. & Cuvier, O. Predicting the spatial organization of chromosomes using epigenetic data. *Genome Biol.* **16**, 182 (2015).
42. Zhang, Y. et al. Transcriptionally active HERV-H retrotransposons demarcate topologically associating domains in human pluripotent stem cells. *Nat. Genet.* **51**, 1380–1388 (2019).
43. Zhang, S. et al. RNA polymerase II is required for spatial chromatin reorganization following exit from mitosis. *Sci. Adv.* **7**, eabg8205 (2021).
44. Krietenstein, N. et al. Ultrastructural details of mammalian chromosome architecture. *Mol. Cell* **78**, 554–565.e557 (2020).
45. Genga, R. M. J. et al. Single-Cell RNA-Sequencing-Based CRISPRi screening resolves molecular drivers of early human endoderm development. *Cell Rep.* **27**, 708–718.e710 (2019).
46. Dekker, J., Rippe, K., Dekker, M. & Kleckner, N. Capturing chromosome conformation. *Science* **295**, 1306–1311 (2002).
47. Engreitz, J. M. et al. RNA-RNA interactions enable specific targeting of noncoding RNAs to nascent Pre-mRNAs and chromatin sites. *Cell* **159**, 188–199 (2014).
48. Rahl, P. B. et al. c-Myc regulates transcriptional pause release. *Cell* **141**, 432–445 (2010).
49. Chao, S. H. & Price, D. H. Flavopiridol inactivates P-TEFb and blocks most RNA polymerase II transcription in vivo. *J. Biol. Chem.* **276**, 31793–31799 (2001).
50. Barutcu, A. R., Blencowe, B. J. & Rinn, J. L. Differential contribution of steady-state RNA and active transcription in chromatin organization. *EMBO Rep.* **20**, e48068 (2019).
51. Jain, A. & Vale, R. D. RNA phase transitions in repeat expansion disorders. *Nature* **546**, 243–247 (2017).
52. Saha, S. & Hyman, A. A. RNA gets in phase. *J Cell Biol.* **216**, 2235–2237 (2017).
53. Aumiller, W. M. Jr. & Keating, C. D. Phosphorylation-mediated RNA/peptide complex coacervation as a model for intracellular liquid organelles. *Nat. Chem.* **8**, 129–137 (2016).
54. Brahma, S. & Henikoff, S. RNA Polymerase II, the BAF remodeler and transcription factors synergize to evict nucleosomes. *bioRxiv* <https://doi.org/10.1101/2023.01.22.525083> (2023).
55. Ilik, I. A. et al. SON and SRRM2 are essential for nuclear speckle formation. *Elife* **9** <https://doi.org/10.7554/eLife.60579> (2020).
56. Fu, X. D. & Maniatis, T. Factor required for mammalian spliceosome assembly is localized to discrete regions in the nucleus. *Nature* **343**, 437–441 (1990).
57. Smith, K. P., Hall, L. L. & Lawrence, J. B. Nuclear hubs built on RNAs and clustered organization of the genome. *Curr. Opin. Cell Biol.* **64**, 67–76 (2020).
58. Kim, J., Han, K. Y., Khanna, N., Ha, T. & Belmont, A. S. Nuclear speckle fusion via long-range directional motion regulates speckle morphology after transcriptional inhibition. *J. Cell Sci.* **132** <https://doi.org/10.1242/jcs.226563> (2019).
59. Sigova, A. A. et al. Transcription factor trapping by RNA in gene regulatory elements. *Science* **350**, 978–981 (2015).
60. Henninger, J. E. et al. RNA-mediated feedback control of transcriptional condensates. *Cell* **184**, 207–225.e224 (2021).

61. Durand, N. C. et al. Juicer provides a one-click system for analyzing loop-resolution Hi-C experiments. *Cell Syst.* **3**, 95–98 (2016).
 62. Subramanian, A. et al. Gene set enrichment analysis: a knowledge-based approach for interpreting genome-wide expression profiles. *Proc. Natl. Acad. Sci. USA.* **102**, 15545–15550 (2005).
 63. Gonzalez, F. et al. An iCRISPR platform for rapid, multiplexable, and inducible genome editing in human pluripotent stem cells. *Cell Stem Cell* **15**, 215–226 (2014).
 64. Zufferey, M., Tavernari, D., Oricchio, E. & Ciriello, G. Comparison of computational methods for the identification of topologically associating domains. *Genome Biol.* **19**, 217 (2018).
 65. Liang, L. et al. Complementary Alu sequences mediate enhancer-promoter selectivity. *Nature* **619**, 868–875 (2023).
 66. Wen, X. & Zhong, S. Alu transposable elements rewire enhancer-promoter network through RNA pairing. *Mol. Cell* **83**, 3234–3235 (2023).
 67. Yesbolatova, A. et al. The auxin-inducible degron 2 technology provides sharp degradation control in yeast, mammalian cells, and mice. *Nat. Commun.* **11**, 5701 (2020).
 68. Abdennur, N. & Mirny, L. A. Cooler: scalable storage for Hi-C data and other genomically labeled arrays. *Bioinformatics* **36**, 311–316 (2020).
 69. Kerpedjiev, P. et al. HiGlass: web-based visual exploration and analysis of genome interaction maps. *Genome Biol.* **19**, 125 (2018).
 70. Crane, E. et al. Condensin-driven remodelling of X chromosome topology during dosage compensation. *Nature* **523**, 240–244 (2015).
 71. Wienert, B., Shin, J., Zelin, E., Pestal, K. & Corn, J. E. In vitro-transcribed guide RNAs trigger an innate immune response via the RIG-I pathway. *PLoS Biol.* **16**, e2005840 (2018).
 72. Miele, A., Gheldof, N., Tabuchi, T. M., Dostie, J. & Dekker, J. Mapping chromatin interactions by chromosome conformation capture. *Curr. Protoc. Mol. Biol.* **11** <https://doi.org/10.1002/0471142727.mb2111s74> (2006).
 73. Miele, A. & Dekker, J. Mapping cis- and trans- chromatin interaction networks using chromosome conformation capture (3C). *Methods Mol. Biol.* **464**, 105–121 (2009).
 74. Lu, L. et al. Robust Hi-C Maps of Enhancer-Promoter Interactions Reveal the Function of Non-coding Genome in Neural Development and Diseases. *Mol. Cell* **79**, 521–534.e515 (2020).
 75. Zhang, S. et al. DeepLoop robustly maps chromatin interactions from sparse allele-resolved or single-cell Hi-C data at kilobase resolution. *Nat. Genet.* **54**, 1013–1025 (2022).
- DP1HD087990 (S.Z.), R01HD107206 (S.Z.), R01GM136922 (W.L.), and NIH Common Fund 4D Nucleome grants UM1HG011593 (J.M.), UM1HG011585 (B.R.), U54DK107977 (B.R.), U01HL156059 (W.L.), U01CA200147 (S.Z.).

Author contributions

R.C., X.W., and S.Z. conceived the project. J.L.C.R., Z.L., T.C.N., C-J.C., S.X., W.W., K.Z.R., R.H., M.Y., W.L. carried out the experiments. R.C., X.W., Z.Q., W.C., Z.Y., and Y.W. carried out the data analysis. R.C., X.W., J.L.C.R., T.C.N., C-J.C., Z.Q., W.C., Z.Y., W.L., J.M., B.R., S.Z. contributed to the interpretation of the results. R.C., X.W., and S.Z. took the lead in writing the manuscript. J.L.C.R., W.L., J.M., and B.R. provided critical feedback and helped to shape the research, analysis and manuscript.

Competing interests

B.R. is a co-founder and consultant for Arima Genomics, Inc. and co-founder of Epigenome Technologies. S.Z. is a founder of Genemo, Inc. W.L. is a co-founder of Hub Biosciences (Houston). The remaining authors declare no competing interests.

Additional information

Supplementary information The online version contains supplementary material available at <https://doi.org/10.1038/s41467-023-42274-7>.

Correspondence and requests for materials should be addressed to Sheng Zhong.

Peer review information *Nature Communications* thanks the anonymous reviewers for their contribution to the peer review of this work. A peer review file is available.

Reprints and permissions information is available at <http://www.nature.com/reprints>

Publisher's note Springer Nature remains neutral with regard to jurisdictional claims in published maps and institutional affiliations.

Open Access This article is licensed under a Creative Commons Attribution 4.0 International License, which permits use, sharing, adaptation, distribution and reproduction in any medium or format, as long as you give appropriate credit to the original author(s) and the source, provide a link to the Creative Commons licence, and indicate if changes were made. The images or other third party material in this article are included in the article's Creative Commons licence, unless indicated otherwise in a credit line to the material. If material is not included in the article's Creative Commons licence and your intended use is not permitted by statutory regulation or exceeds the permitted use, you will need to obtain permission directly from the copyright holder. To view a copy of this licence, visit <http://creativecommons.org/licenses/by/4.0/>.

© The Author(s) 2023

Acknowledgements

We thank 4DN Data Coordination and Integration Center for hosting the raw and the preprocessed datasets for public access. We thank the 4DN Cell Working Group, 4DN Omics Standards Working Group, and 4DN Steering Committee for providing guidelines on experimental protocols and data processing pipelines. We thank the 4DN Joint Analysis Working Group for evaluation of all the data in this resource and cross-comparison with the other 4DN Consortium generated datasets. This work is funded by NIH grants DP1DK126138 (S.Z.), R01GM138852 (S.Z.),